metals

MDPI

Article

Strains and Stresses in Multilayered Materials Determined Using High-Energy X-ray Diffraction

Guillaume Geandier [1,*,†], Patrick Adenis [2], Serge Selezneff [3], Quentin Pujol d'Andredo [2] and Benoît Malard [4,†]

[1] Institut Jean Lamour, UMR CNRS 7198, Université de Lorraine, 54000 Nancy, France
[2] SAFRAN Aircraft Engines, Site de Villaroche, 77550 Moissy-Cramayel, France;
[3] Safran Tech, Rue des Jeunes Bois, Chateaufort CS 80112, 78772 Magny Les Hameaux, France
[4] Le Centre Interuniversitaire de Recherche et d'Ingénierie des Matériaux (CIRIMAT), Université de Toulouse, CNRS, INPT, UPS, 4 Allèe Emile Monso, CS 44362, CEDEX 4, 31030 Toulouse, France; benoit.malard@toulouse-inp.fr
* Correspondence: guillaume.geandier@univ-lorraine.fr; Tel.: +33-372742728
† These authors contributed equally to this work.

Abstract: This work explores the advantages and disadvantages of a methodology using high-energy X-ray diffraction to determine residual stresses in multilayer structures produced by atmospheric plasma spraying. These structures comprise a titanium alloy substrate (Ti64), a bonding layer (Ni-Al), and an abrasive coating (Al_2O_3). This study focuses on analyzing the residual stress gradients within these layers. The presented method is used to determine stresses across the entire thickness of multilayer structures. Experiments were carried out using a high-energy rectangular beam, operating in transmission mode, on the cross-section of the sample. The results indicate variable stresses throughout the depth of the sample, particularly near the layer interfaces. The semi-automatic methodology presented here enables us to follow stress evolution within the different layers, providing indications of the load transfer between them and at their interfaces. The $\sin^2\psi$ method was used to analyze the diffraction data and to determine the stresses in each phase along the sample depth. However, interpreting results near the interfaces is complex due to the geometric and chemical effects. We present a discussion of the main advantages and disadvantages of the methodology for this kind of industrial sample.

Keywords: strain; stress; X-ray diffraction; high-energy X-ray; multilayer material

check for updates

Citation: Geandier, G.; Adenis, P.; Selezneff, S.; Pujol d'Andredo, Q.; Malard, B. Strains and Stresses in Multilayered Materials Determined Using High-Energy X-ray Diffraction. *Metals* **2024**, *14*, 637. https://doi.org/10.3390/met14060637

Academic Editor: Matteo Benedetti

Received: 17 April 2024
Revised: 16 May 2024
Accepted: 24 May 2024
Published: 27 May 2024

Copyright: © 2024 by the authors. Licensee MDPI, Basel, Switzerland. This article is an open access article distributed under the terms and conditions of the Creative Commons Attribution (CC BY) license (https://creativecommons.org/licenses/by/4.0/).

1. Introduction

The atmospheric plasma spraying (APS) technique is widely employed to produce various protective coatings for heat-, wear-, and corrosion-resistant surface layers [1]. Made from a variety of materials, such as metals, ceramics, and polymers, these coatings involve introducing powdered material into a plasma flame. This process melts the particles and propels them onto the substrate to be coated. The particles' impact results in their flattening, cooling, and solidification, thus forming a solid layer. Due to porosity, anisotropy, and residual stresses, the properties of these coatings differ significantly from bulk materials of the same composition [2]. These stresses are primarily caused by significant temperature variations during the deposition process.

When the molten particles reach the substrate, they rapidly cool, creating a tensile stress within the coating known as "quenching stress" [3]. During deposition, the substrate is kept at a low temperature (<150 °C by blowing), while post-deposition cooling creates thermal stress due to differences in the coefficients of thermal expansion (CTE) between the coatings and the substrate. These quenching and thermal stresses are the main sources of residual stress. Elevated stresses can lead to various issues, such as cracking, spalling or dimensional changes, thereby compromising the component's overall performance. Therefore, understanding the evolution of these stresses is crucial for assessing their impact

on the lifespan and functionality of the component, as well as for controlling them by modifying the coating [2]. In the case of multilayer structures, layer growth can result in deformation and stress gradients, requiring an adapted experimental approach. It is also essential to consider non-linear phenomena, such as delamination and cracking. The sharp interface between the two layers, however, is generally the most frequent site of failure. This has led to investigations into graded coatings [4–7], with compositions continuously varying from pure metal to pure ceramic, in order to make the interface more 'diffused' and thereby reduce stress discontinuity. Therefore, it is crucial to understand the spatial scales accessible with different characterization tools and compare them to modeling scales.

Several methods exist for determining these stresses [8], including mathematical modeling, material removal techniques [9], mechanical methods [10,11], spectroscopic methods [12,13], and diffraction methods [14]. Each technique has its advantages and limitations, and the choice depends on various factors, such as the shape and dimensions of the sample, as well as the availability of necessary equipment. Among these tools, neutron diffraction offers several advantages, including non-destructiveness and the ability to determine stresses in each phase of a composite. Laboratory X-ray diffraction can also be used, but it can only determine stresses in a thin surface layer (several microns) and requires successive material removal. The curvature method, on the other hand, enables the in situ non-destructive determination of stresses in thick layers [15].

In this paper, a high-energy X-ray diffraction (HEXRD) method was used to determine residual stresses in each phase, enabling precise measurements across the entire thickness of fixed-composition multilayer structures. Here, we focus on the advantages and disadvantages of a methodology for determining residual stress gradients in an industrial metal (Ti64)/interlayer (Ni-5 wt.% Al)/abrasive coating material (Al_2O_3 with 3 wt.% TiO_2) system via APS thermal spraying.

2. Materials and Methods

2.1. Materials

The components under investigation, referred to as labyrinth seal fins, are positioned within a high-pressure (HP) aircraft turbojet engine compressor. These labyrinth seal fins play a crucial role in enhancing rotor–stator contact conditions and optimizing engine sealing. However, aerodynamic flow conditions in the jet engine often lead to vibratory instability phenomena, consequently impacting engine performance [16]. As an initial step, we simplified the geometry of the problem by substituting labyrinth seal fins with plates, facilitating in-plane deformation measurements. The dimensions of these plates are $5 \times 5 \times 2$ mm^3. Manufactured using APS, the plates consist of three distinct layers: a substrate (Ti64) with a thickness exceeding 1.5 mm, a bonding layer (Ni-5 wt.% Al) that is approximately 150 µm thick, and an abrasive coating (Alumina-3 wt.% TiO_2) that is around 350 µm thick. Notably, a significant thickness irregularity is observed at the bound coat–abrasive coating interface (Figure 1).

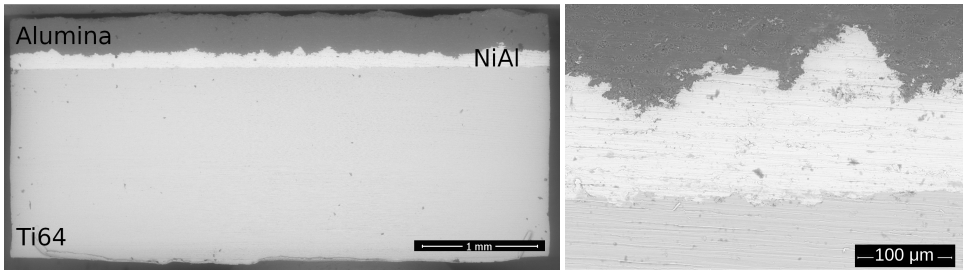

Figure 1. (**left**) Global view of the different layers: (dark grey) Ni-Al, (white) alumina, (light gray) Ti64, (**right**) zoom on the alumina–NiAl interface layers.

Composed of Ti64, the substrate is a widely used titanium alloy recognized for its hexagonal alpha (α) and cubic-centered beta (β) grain microstructure, resulting from precise

heat treatment. This combination imparts excellent mechanical strength, low density, and good corrosion resistance, which is why Ti64 is extensively utilized in the aerospace and medical industries, as well as for other applications requiring an optimal balance between lightness and mechanical strength. Its physical properties, including thermal conductivity and coefficient of thermal expansion, make it a versatile material for various industrial applications.

The bonding layer employs Ni-5 wt.% Al, a two-phase γ-γ' alloy with 89.7% atomic nickel and 10.3% aluminium. The mechanical, physical, and thermo-mechanical properties of this alloy are influenced by the microstructure formed during different types of thermal spraying. The presence of inter-lamellar pores contributes to the porous microstructure (10%) of the metal alloy.

The abrasive coating material is alumina, a widely used ceramic known for its chemical stability and high hardness. Alumina undergoes various phase transformations during APS, with the majority observed after deposition in the γ phase.

The addition of 3 wt.% TiO_2 enhances the toughness of alumina deposits. The ceramic is subjected to a thermal treatment characterized by stages such as melting, acceleration, cooling, and deceleration in the plasma jet, as well as spreading on the substrate and solidification [17–20].

2.2. Plasma Spraying

Plasma spraying, a thermal spraying process, involves projecting solid, molten, or softened particles onto a prepared surface using a heat source. The APS process, conducted at atmospheric pressure, is advantageous for melting high-melting-point materials like refractory metals and ceramics. According to Sampath et al., during APS, the grouping of spread particles, known as "flocs", is fragmented. This fragmentation is due to the low viscosity of the fluid (sprayed particles) impacting the solid substrate [2]. In addition, the metal alloy has a porous microstructure with inter-lamellar pores. Formed particle-by-particle, the resulting deposit exhibits a more or less lamellar structure (Figure 2).

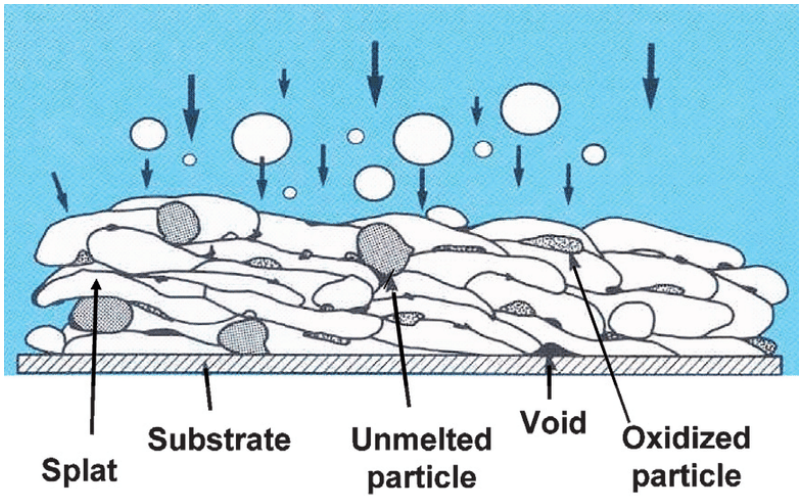

Figure 2. Structure of a plasma-sprayed deposit (reprinted from Ref. [21]).

Studies have highlighted the impact of APS process parameters, including arc plasma power, plasma gas type, deposition distance, and powder transport speed, on the microstructures of deposits. The lamellar structure and porosity (ranging from 1 to 25%) in plasma-sprayed deposits are influenced by these parameters and the materials used. Residual stresses, originating from rapid cooling and differences in coefficients of thermal expansion between layers, are introduced during thermal spray processes. The cooling process significantly affects coating quality, influencing properties via the microstructure.

This work aims to propose a methodology for analyzing the residual stress states in the various layers comprising representative plates after manufacture. We will also discuss the method's limitations.

2.3. HEXRD—sin²ψ

The HEXRD experiments were performed at the ESRF ID 11 beamline (ESRF, Grenoble, France). The high-energy rectangular beam (E = 80.0 keV, 300 × 5 μm^2) allowed us to work in transmission mode on the cross-section of the sample with the following dimensions: 5 × 5 × 2 mm^3. During the experiments, the sample was moved step-by-step along the z-axis (2 μm step size). A 2D FReLOn detector (2048 × 2048 pixels, pixel size of 50 × 50 μm^2) allowed us to record 2D images of a diffracted volume of 300 × 5 × 5000 μm^3 at every step. Figure 3 presents a schematic view of the setup used during the experiment and a photograph of the sample on the goniometer.

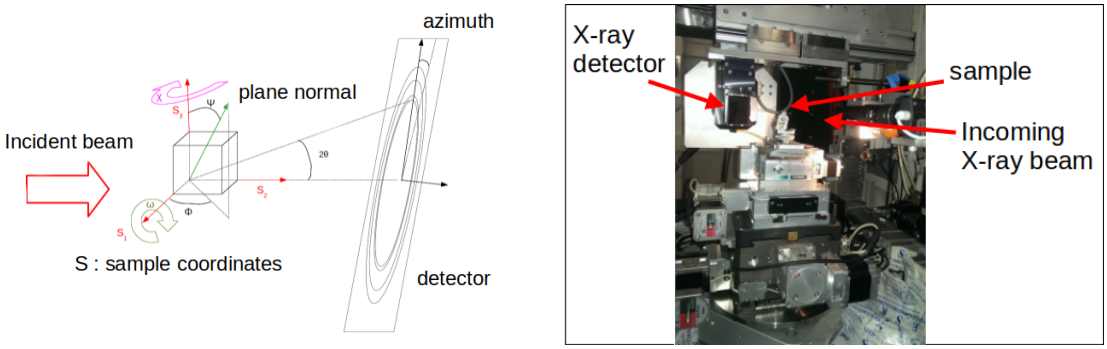

Figure 3. (**left**) Experimental setup used at ID11. (**right**) Photograph of one sample placed on the goniometer.

In order to place the beam at the center of the specimen and align it with the top surface of the sample (ω angle in Figure 3), a series of absorption and reflective scans were conducted by using the direct beam and a photodiode positioned behind the sample. To perform the alignment, we used translations (x, y, and z, with x and y as the horizontal plane and z along the sample depth, perpendicular to the layers), rotations, and directions perpendicular to the incoming beam. The 2D detectors used to sample the distance and the detector tilts were calibrated using a silicon powder diffraction and pyFAI software [22] suite [23].

The results were analyzed using the sin$^2\psi$ method, as described in [24], where an adaptation of the sin$^2\psi$ [25] for HEXRD data is presented. Then, 2D images were integrated using pyFAI suite software with 1° caking. Two directions (ϕ angle, 0 and 90°, rotation around the vertical axis) were investigated. Selected peaks for each phase were adjusted using the Pearson VII function with a local linear background. As samples were composed of multiple materials, a peak for each phase was selected based on significant intensities, consideration of the degree of overlapping (inside each layer and at the interfaces), and the mechanical anisotropy of the hkl Miller indices of possible peaks.

Similar procedures have been used in similar studies on other beamlines, for example, in [26–28].

3. Results

3.1. Diffraction—Phases

Diffraction images were recorded from outside the sample and inside up to the titanium alloy substrate. Figure 4 presents 2D images of the three layers. The rings are continuous and no intensity modulations are visible. This means that the grain sizes (crystallites) are small enough to assume a powder diffraction condition and that no texture is present in the different layers. Figure 5 presents a series of diffractograms from the top surface of the substrate for the two ϕ directions investigated. For both directions, three

constitutive layers can be clearly identified. Close to the surface, a layer mainly comprising alumina can be detected; the bound coat layer comprises NiAl and the substrate layer is based on a titanium alloy. In the substrate layer, the diffraction peaks from both phases (α and β) can be identified.

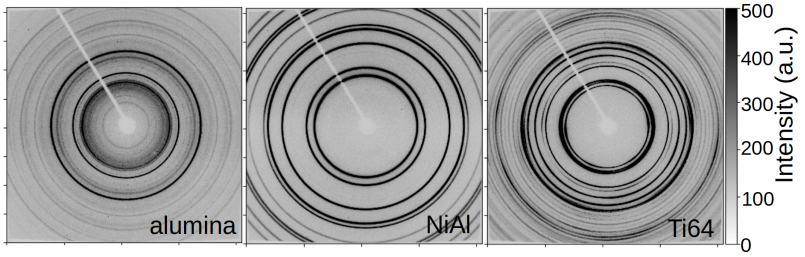

Figure 4. XRD diffraction signals of (from **left** to **right**) abrasive alumina coat, NiAl bound coat, and Ti64 substrate.

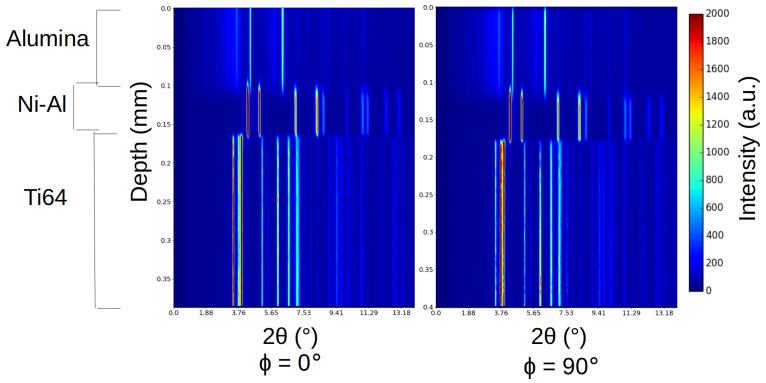

Figure 5. A 2D XRD representation map of diffractograms as a function of depth and for the two ϕ directions.

From the XRD images and integrations, the main phases can be identified: α and γ alumina, NiAl, and α and β titanium. Low-amount phases cannot be detected (TiO_2 in alumina, for example).

3.2. Diffraction—$sin^2\psi$

The $\sin^2\psi$ method was used to determine the strain in the different phases and along the sample depth. With a step of 1°, 2D images were integrated along the δ direction (δ is the azimuth along the rings). The $\sin^2\psi$ method is applied without a hypothesis regarding the strain and stress field shape. To apply this method, each image is integrated to 360 diffractograms. For each diffractogram, one peak for each phase is fitted with a Pearson VII function and local linear background in order to extract the position, intensity, FWHM, and shape parameter, as well as the background coefficients.

Using the position of each peak for each step, $\sin^2\psi$ curves are analysed using the ψ and ϕ angle values calculated from the relation developed in [29]. From the peak position, strain in various directions (ϕ, ψ) can be calculated using Equation (1). ϕ is the rotation around the vertical axis of the sample and ψ is the angle between the vertical axis of the sample and the normal crystallographic plane. θ and d_{hkl} are related to the measured peak positions and θ_0 and d_0 are related to the stress-free peak positions.

$$\epsilon_{\phi\psi} = ln\frac{sin\theta_0}{sin\theta} \simeq \frac{d_{hkl} - d_0}{d_0} \quad (1)$$

The relationship between strain and stress is presented in Equations (2) and (3):

$$\epsilon_{\phi\psi} = \frac{1}{2}S_2[(\sigma_\phi - \sigma_{33})sin^2\psi + \sigma_{33} + (\sigma_{13}cos\phi + \sigma_{23}sin\phi)sin2\psi] + S_1(\sigma_{11} + \sigma_{22} + \sigma_{33}) \quad (2)$$

$$\sigma_\phi = \sigma_{11} cos^2\phi + \sigma_{22} sin^2\phi + 2\sigma_{12} sin\phi cos\phi \quad (3)$$

S_1 and $\frac{1}{2}S_2$ are the radio-elastic coefficients. They are determined from the mechanical properties of the bulk materials:

$$S_1 = -\frac{\nu}{E} \quad (4)$$

$$\frac{1}{2}S_2 = \frac{(1+\nu)}{E} \quad (5)$$

where E and ν are Young's modulus and Poisson's ratio.

From the $\sin^2\psi$ curves (see Figure 6), different information can be extracted:

- If the shape is an ellipsoid, shear stress may be present. A linear shape means that shear stress may be neglected in the analysis. Weaknesses in this shape provide information regarding the microstructure as a texture or gradient in the diffracting volume.
- From the intercept, the strain evolution in one direction (depending of the experimental geometry) can be evaluated.
- From the slope and intercept, the strain evolution in all directions can be evaluated.

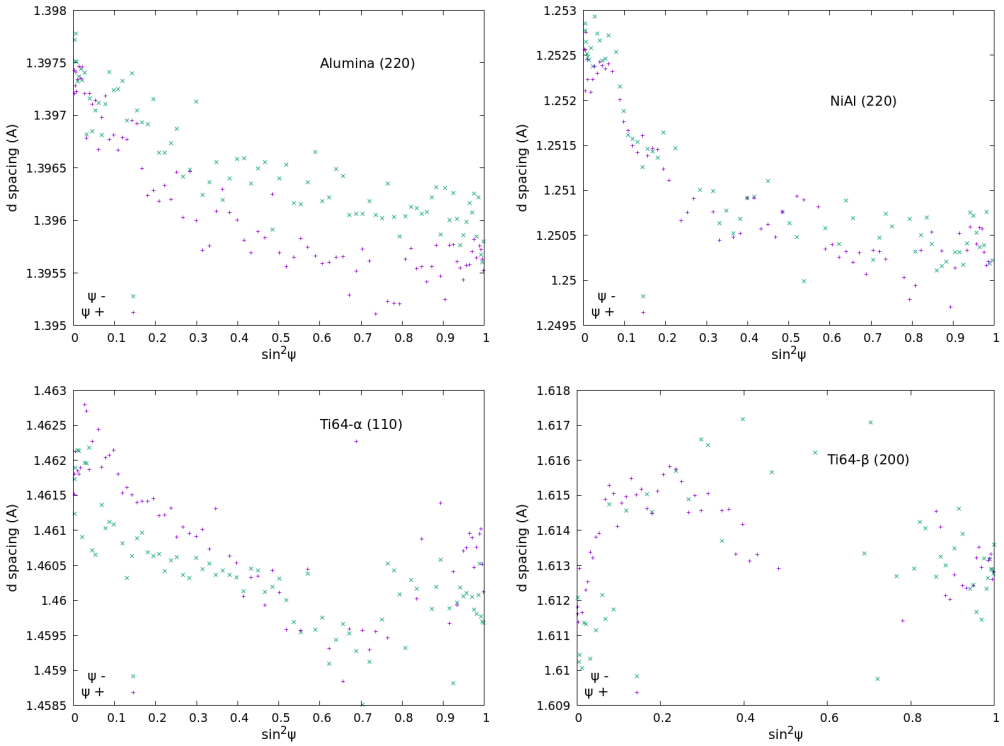

Figure 6. Examples of $\sin^2\psi$ curves for each phase and ellipse opening evolution. Data for Ti64 alloys are extracted from the same depth (same image).

Figure 6 presents selected $\sin^2\psi$ curves for each phase in the sample. These curves are representative of the shape of curves along the depth of the sample, except some points close to the interfaces where the shape shows that some gradients may be present in the diffracting volume. For the strain/stress analysis, the shear strain/stress will be neglected due to the linear shape of the curves and low values of the ellipse opening. Figure 7 presents the evolution of the intercept and slope of $\sin^2\psi$ in each phase along the depth for both ϕ directions.

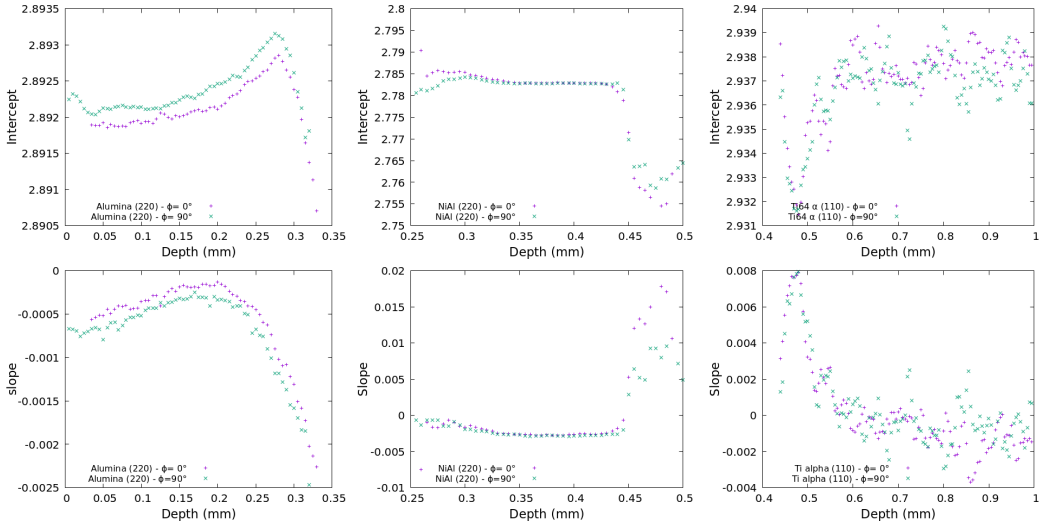

Figure 7. Evolution of intercept and slope for each phase as a function of depth from the sample surface.

From the intercept and slope evolution, the strain and stress can be extracted using Equations (6)–(8).

$$\epsilon_{33} = Intercept - ln(\frac{1}{sin\theta_0}) \tag{6}$$

$$\sigma_{11} - \sigma_{33} = \frac{E_{hkl}}{1 + \nu_{hkl}}.Slope_{\phi=0} \tag{7}$$

$$\sigma_{22} - \sigma_{33} = \frac{E_{hkl}}{1 + \nu_{hkl}}.Slope_{\phi=90} \tag{8}$$

Indices 11, 22, and 33 are related to the sample directions. For the present study, 33 represents the direction normal to the sample surface and 11 and 22 are related to the in-plane strain/stress directions. From the recorded data, ϵ_{33} can be determined for the dataset for the two ϕ directions. In Figure 7, some differences between the two ϕ directions can be observed. These differences are related to the small misalignment of the sample for both directions; these were corrected in the calculation by using the calibration powder (stress-free powder) to a corrected 2θ position for the sample. The difference between the attended and measured positions of the calibrant peaks were applied to the phase peaks, considering those closest.

3.3. Strain–Stress

The stress-free parameters were extracted from the powder diffractograms. Measurements were made on a beamline ID22 [30] at the ESRF with a beam energy of 31 keV using the multianalyzer stage. Figure 8 presents the diffractograms of each initial powder. For a NiAl and Ti64 alloy, the bulk structures remain the same as the initial powders (meaning the powders used in the APS process); however, a change is observed for alumina. Figure 9 presents the diffractograms of alumina powder extracted from samples, measured on ID11 under the same conditions as the sample. The initial alumina structure is still present, but the main phase is now γ-alumina. TiO_2 is detected in the initial powder (8) but is not detected in the final mixture, where an amorphous phase is also present (9).

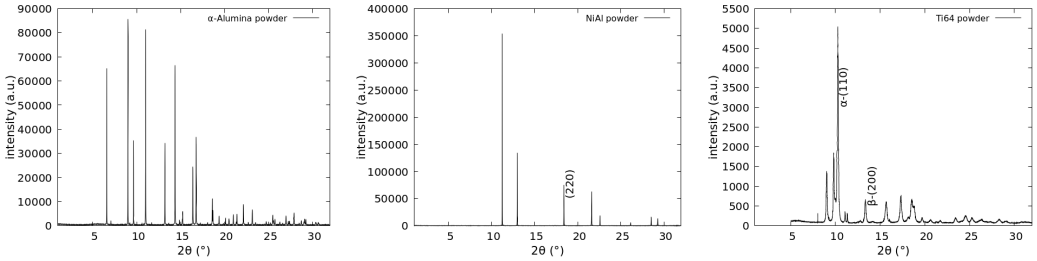

Figure 8. Diffractograms of initial powders obtained at ID22—31 keV (from **left** to **right**: alumina, Ni-Al, Ti64).

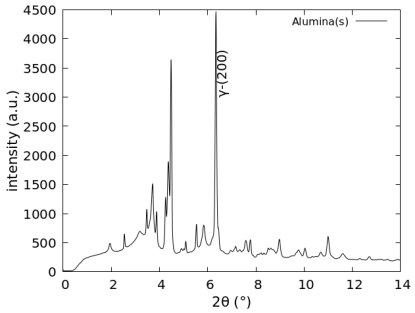

Figure 9. Diffractograms of alumina powder extracted from sample obtained at ID11—80 keV.

From the powder diffraction experiments, stress-free cell parameters for each phase were extracted and one (hkl) plane was selected for strain/stress analysis. For the powders presented in Figure 8, cell parameters were extracted via Rietveld refinement; for the powder in Figure 9, the cell parameter was extracted from a single peak position. Table 1 presents the parameters used for peak selection and the properties of the selected phases.

Table 1. Phase parameters used to determine strain and stresses.

Phases	Space Group	σ-Free Cell Parameters (Å)—(hkl)	Macroscopic Mechanical Properties (E in GPa and ν)
γ-alumina	F d $\bar{3}$ m	3.9533—(220)	253—0.24 [31]
NiAl	F m $\bar{3}$ m	3.5457—(220)	140—0.25 [32]
Ti64 α	P 6_3/m m c	2.9385/4.6844—(110)	100—0.29 [33]
Ti64 β	I m $\bar{3}$ m	3.2531—(200)	80—0.25 [34]

After applying the method described in the previous section, the stresses in each phase can be determined. Figure 10 presents stress evolution versus depth for all the main phases.

From the stress evolution along the depth, it can be seen that the stress levels are mainly stable in all phases when the considered position is far from the interface. At the interface (alumina-NiAl) and (NiAl-Ti64), strong stress evolution levels are detected in all directions. Also, in the Ti64 part, the results appear more noisy compared to the alumina and NiAl phases. This "noise" can be attributed to the microstructure, in which the fraction of the β phase is low (<10 wt%).

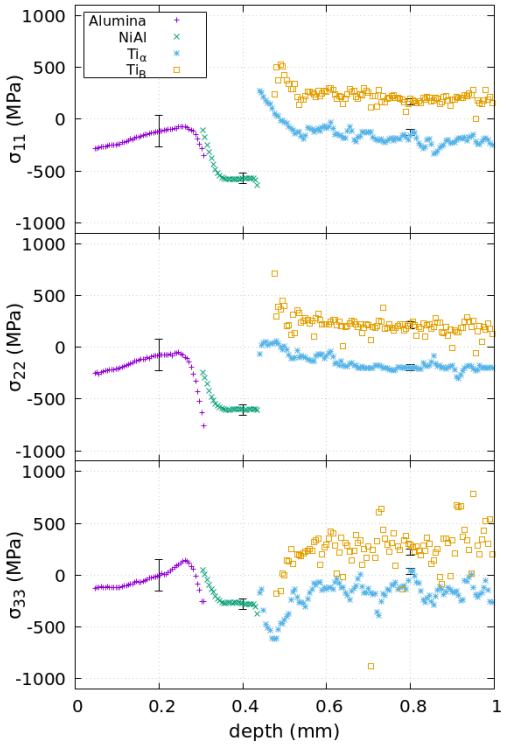

Figure 10. XRD stresses of the layered material.

4. Discussion

4.1. Multiphased Materials

The stresses determined in the different layers (Figure 10) were calculated using the $\sin^2\psi$ method established for isotropic materials. When materials are isotropic at different scales, the values determined by $\sin^2\psi$ give assured results [24]. Most of the time, when dealing with layered multimaterials, the isotropic hypothesis is not valid. This is particularly the case at the interfaces between materials. In the labyrinth seal fin case, this affects the stress evolution across the interface. Figure 1 shows the alumina–NiAl interface with high roughness and Figure 10 presents decreased stress in the alumina layer and an increase in the NiAl layer. This evolution may only be due to the layer repartition along the beam path across the interface, as the beam intercept segmented volume of the different layers, as well as the diffracted signal, are affected by the phase strain but also the beam path position. The convolution of the strain and position may affect the final peak position, which is an average of all the effects. So, it is difficult to conclude if stresses at the alumina–NiAl interface can really change and affect the mechanical performance of the materials; the microstructure may have a more significant impact. For comparison, the results across the Ni-Al/Ti64 interface are sharp and do not present stress evolution in each phase. A sharp transition between phases has no effect on stress.

This example highlights the need for a very deep understanding of the materials at different scales to understand the stress evolution as determined by XRD.

4.2. High-Energy X-ray Diffraction

The high-energy X-ray diffraction (HEXRD) method was selected due to the size of the samples and as representative of the bulk. The choice of beam energy was in accordance with the phase absorption. Figure 11a presents the evolution of the transmitted intensity as a function of the beam path length for the different phases present in the sample, with a beam energy of 80 keV. The evolution shows that the NiAl phase is highly absorbent. The final choice of beam energy is based first on both the beamline capability [35] and on the absorption in relation to the sample width, as illustrated in Figure 11b. At

80 keV, a small part of the intensity is transmitted and coupled with the high flux from the synchrotron beamline; the diffracted signal and signal over noise are strong to allow for strain/stress analysis.

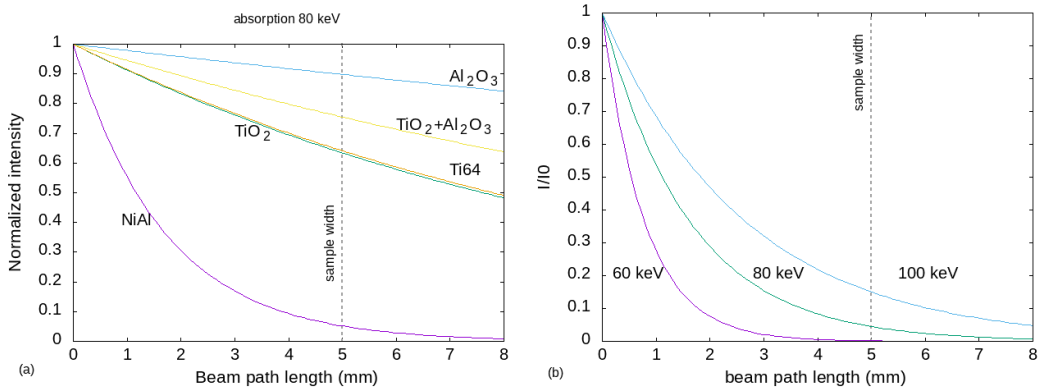

Figure 11. (**a**) Absorption calculation of the different layers at 80 keV. (**b**) Absorption of NiAl layer for energy between 60 and 100 keV.

For determining strain and stress with a monochromatic beam on samples with a complex shape or a high dimension, one major point to consider during experimental design is the diffracting volume. As diffraction affects the whole beam path in the sample, the setup must be adjusted to ensure that the investigated volume is representative of the microstructure. This path may be different when diverse directions are considered, as in the case of our samples. Here, plates were used, but their dimensions along the beam direction can be large compared to others directions. So, the diffracting volume is different, and only one small part is shared by both of the two considered ϕ directions: ($300 \times 300 \times 5$ µm^3) compared to ($5000 \times 300 \times 5$ µm^3) for one beam path (see Figure 12). In the present case, previous analysis has shown that the samples' microstructures are stable, so there is no significant difference from one path to another. Differences can be observed, however, close to the interfaces, as the phase continuities are dependent on the surface rugosity.

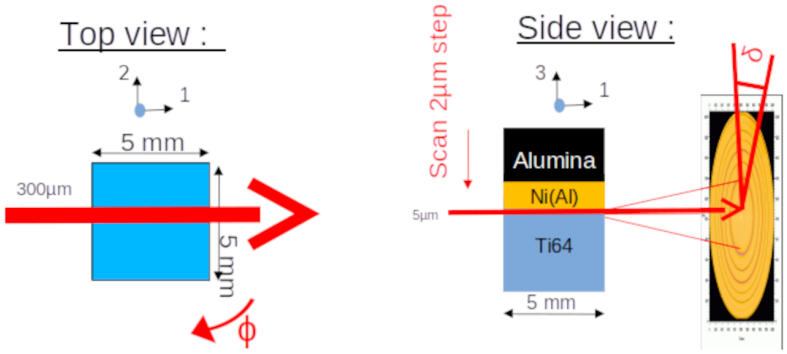

Figure 12. Illustration of beam path in the sample.

As illustrated in Figure 12, the diffracting signal is extracted for the whole beam path in the sample. This means that the peak used for strain calculation is an average of the complete sample width. This peak is the convolution of the signal from the sample parts positioned in the bulk (i.e., the sample's center), as well as the free surface at the start and end of the beam path. The presence of a free surface is conducive to strain and stress relaxation, which will ultimately affect the results. For an equivalent setup, the relaxation effect was evaluated during another experimental session at P07 (DESY, Hamburg, Germany) [28] by making scans with an equivalent beam shape but placed at the edge of a sample, where the effect of the free surface is maximized along the beam path. By analyzing the peak position from the full free surface to the center, the results show that the free surface affects an area of 200 µm and can decrease the strain value by 10%.

4.3. Sin²ψ Method

From synchrotron experiments, users accumulate a lot of raw data. With this experiment, one sample represents 420 2D images (5 Go of raw data). With the selected methodology with caking of 1°, four phases in the sample were investigated in order to analyze 1,800,000 individual diffraction peaks. Of course, this was achieved with adapted algorithms and not by hand; the latter has been impossible for years. But, with the huge amount of data (some recent experiments are much bigger [26–28], with up to 12,000 2D images and 200 Go of raw data per sample), one critical point is data verification. For several reasons (bad image quality, choice of parameters, beam loss, bad pixels, unexpected microstructure evolution, low phase amounts . . .), the results from all steps can produce bad data that must be revoked between steps to avoid biased interpretation. These revocation steps become crucial when using algorithms on large datasets (they are even more crucial when using "black boxes" codes or softwares). In our methodology, after peak fitting, data are scanned and the limitations of several parameters are tested. All data that fall outside these limits are revoked and not taken into account. This can result in there not being enough data for analysis; in this particular case, more investigations from users must be performed to identify the problem and change the parameters. In this study, the scanned parameters are as follows:

- The 2θ position that must be within a selected area around the peak.
- Raw intensity that cannot be below one, above the background, or above the detector capacity (2^{16} in the case of the detector used here).
- FWHM that cannot be below one 2θ step higher than a value determined by the user (here, 0.5 is very large compared to the expected values).
- The fit quality factor is the difference between the fitted function (including local background) and raw data regarding the considered interval around the selected peak. This value has a minimum and maximum (1 and 10 here) that represent the quality of fit; a high value means a bad fit and 1 is a perfect fit.

These data selection steps are crucial in assuring quality results, even if a large amount of data is "lost" at this step. Usually, the dataset is large enough and the methodology is adapted to ensure a sufficient amount of data for results extraction.

4.4. Stress-Free Parameters—d_0

Determining stress using XRD may involve many hypotheses for tensor solving. HEXRD, with an adapted experiment, can help to solve the full tensor [24]. However, the main hypothesis is the stress-free value; this has an effect, especially if the objective is to obtain the absolute stress level and not just the evolution. In the labyrinth seal fin case, powders from initial materials or those extracted for treated materials were studied separately and can be used as stress-free parameters. The stress levels determined using these parameters are physically acceptable, meaning that the materials can withstand this kind of stress level and that the values are thus realistic.

Stress-free parameters may be discussed for the alumina layer, as the powder used is not representative of the bulk materials. Powders are a complex material with (at least) three phases: γ, α alumina, and an amorphous phase. For the stress-free parameter, we extracted the value for the main phase in the bulk. The case of alumina illustrates that the industrial process has an effect on the phase evolution; stress-free parameters must not be neglected and must be studied separately. In most cases, it is not possible to use raw powder before treatment. Different methods of obtaining stress-free parameters exist, i.e., by extracting powders from bulk, by combing, or choosing a reference point in the bulk that is free of the investigated stress effects. Each method has its own difficulties.

- Powder: the grains must be small enough, the chemistry has to be the same, and no pollution should be added. The pollution effect may be important in cases where powder is extracted from the bulk; it is thus essential that care is taken with the extraction tool.

- Comb: this method releases stress by cutting the material to obtain small, stress-free volumes with free surfaces. Here, the difficulty lies in determining what happens when the volume near the free surface has a significant impact and where it can be used. The answer, related to the material's microstructure and grain–phase interaction, is not simple. Determining the volume can be tricky in multi-phased materials when the scales between phases are different.
- Reference point: this method is often used when external factors are applied to the materials (tensile tests, thermal treatments). The main difficulty is in ensuring that the chosen point is not really affected by the investigated phenomena. Strain/stress can affect the material over long distances (mm to cm, in some cases). Occasionally, going as far as the experiment allows may not be enough . . . Furthermore, with this method, residual stresses are neglected and this can have an effect on the interpretation; for example, if residual stresses are compressive, the yield stress determined may appear higher than normal and, on the contrary, if they are tensile, failure may appear during the early stages.

As the aim of the method is to determine the stress tensor without a hypothesis regarding its shape and stress level, stress-free parameters play a crucial role in the final level of stress in each phase.

4.5. Experimental Error

Due to the method used to determine the strains, errors are linked to the experimental resolution.

These errors are estimated based on the peak position dispersion of the calibration powder, which is stress-free and used to precisely determine the distance between the sample and detector, as well as the latter's orthogonality. Looking to the dispersion on the peak position of the calibrant allows us to determine the minimum strain value using the considered setup; this is because the strain is null for the calibrant. For the considered setup, the minimum strain values are between 0.5 and 2 $\times 10^{-4}$ depending on the peak position (2θ), which is related to the number of pixels from the detector matrix that are included in the sector after caking for strain and stress determination.

Errors in the stresses, considering a minimum strain of 2 $\times 10^{-4}$, are estimated as follows: alumina: $\pm$ 150 MPa ; Ni-Al: $\pm$ 50 MPa ; Ti64: $\pm$ 30 MPa.

The alumina phase error seems quite high, but this is due to the high elastic modulus (see Table 1).

Due to the size of the error bars, it was not necessary to increase the methodology's strain resolution. In the case where 2 $\times 10^{-4}$ is insufficient, one simple way to increase the resolution is to correct the peak position by calculating the position error of the calibrant powder. This procedure takes time, as the correction must be calculated and applied on each ring and sector, but the resolution can be increased by a factor of 10 or more depending of the calibrant quality.

Contrary to stress determination using an X-ray tube, the diffraction angle using HEXRD cannot be larger than 15°, as the energy is 10 times higher than common X-ray tubes. The calibration procedure described here allows for minimizing the error in peak positions, as the synchrotron photon flux and detector calibration contribute to reducing the error. This is because the peak intensity over the background is larger than that obtained using X-ray tubes.

4.6. Mechanical Anisotropy, Analyzed Peaks, and Shear Stress

In this study, we made the choice to ignore the mechanical anisotropy on hkl peaks. This decision was driven by the difficulties in selecting phase peaks (multiple peaks in alumina, low phase amount of Tiβ, and overlapping peaks between phases at interfaces). Thus, the main consequence is that the stress level determined in each phase is not representative of the real stress level. It is possible to estimate the effect of mechanical anisotropy and peak selection by using a model to calculate the XEC [25,36]. These coefficients are

hard to obtain experimentally as they are determined via tensile tests on pure compounds. The first difficulty is to obtain pure compounds for each phase of the all materials involved in the final specimen. Once obtained, a tensile test must be carried out in the elastic regime with parameters close to those used in the experiment. In order to illustrate the effect of anisotropy, for cubic symmetry, the XEC was calculated for the classical models, Voigt, Reuss, and Kröner, as a function of the Γ parameter, which is dependent on hkl indices (see Equation (9) for cubic systems).

$$\Gamma = \frac{h^2k^2 + h^2l^2 + k^2l^2}{(h^2 + k^2 + l^2)^2} \tag{9}$$

Figure 13 presents the calculation results for XEC. As expected, the Voigt values are independent of Γ and can be considered as the lower limits; the Reuss model provides the upper limits. For the calculations, S_{ijkl} were estimated from the bulk values given in the article, using formulations described in [36]. Except for the Voigt model, the values of S_1 and $\frac{1}{2}S_2$ increase and decrease, respectively, as Γ increases. The Γ values for the studied strain/stress in the present study are 0.25 for γ–alumina (220) and NiAl (220), and 0.0 for Tiβ (200). The XEC calculated from bulk properties are indicated by black crosses. The XEC used correspond to the highest model values. Taking into account the anisotropy may change the stress levels in each layer.

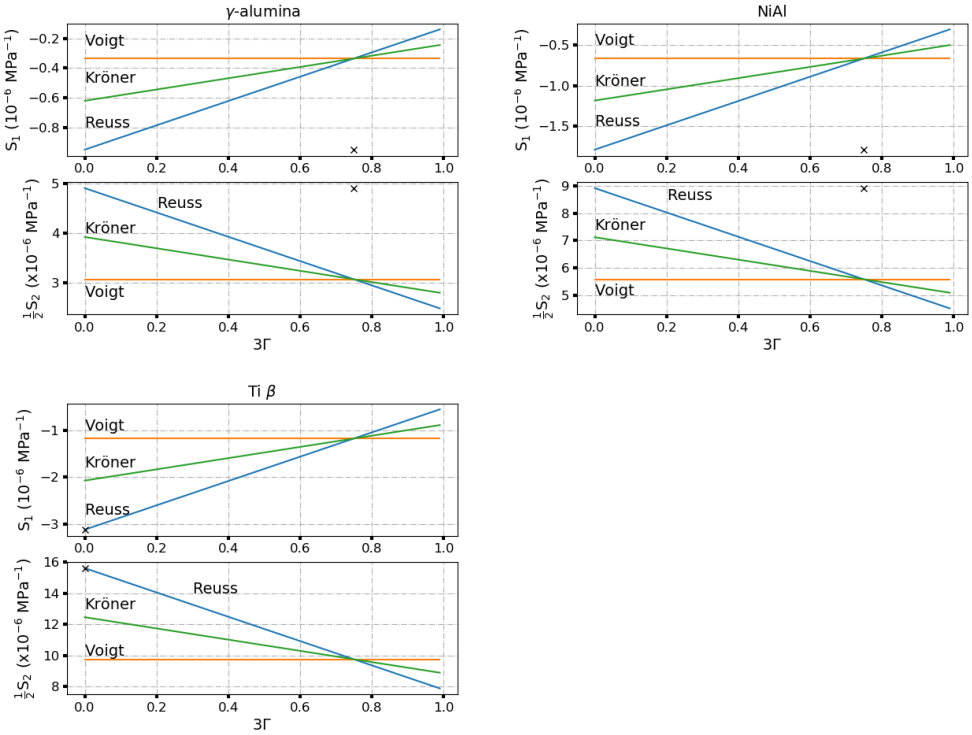

Figure 13. Calculated evolutions versus 3Γ XEC parameter for the three cubic structures in the layered material (lines). XEC used for strain determination are reported as 'x'.

Figure 14 compares the stress levels (σ_{11}) for the XEC calculated from bulk properties and for each model for Γ = 0, where the difference between the models is maximized. As expected, the bulk and Reuss values are very close and values using other XEC exhibit similar behavior but with different stresses. It can be noted that the differences between the different models are not constant along the depth and are dependent on the strain component with a different weight in the stress calculation. The maximum difference in (σ_{11}) for alumina is around 150 MPa, which is the same as the incertitude in this phase (as discussed in Section 4.5). This effect shows that the choice of both XEC and peak (and so anisotropy) is an important point in the analysis. All absolute results are dependent on this choice; meanwhile, the evolution is not affected.

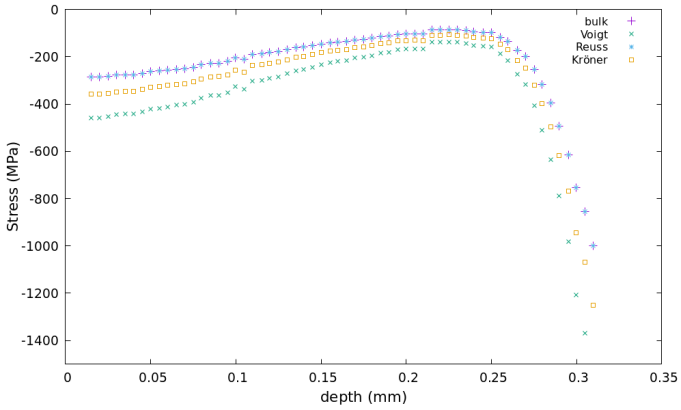

Figure 14. Comparison of σ_{11} determined using XEC from bulk and models (at $\Gamma = 0.0$) for γ-alumina.

It can also be noted that the methodology works well with the specimen, as only diagonal terms of the stress tensor have significant values. As shown in Figure 6, shear stresses are negligible with a negligible opening of the curves. Using the hypothesis that this is true along the depth, we can extract the full strain and stress tensor along the specimen depth. In cases where the hypothesis is not true, the methodology would be inadequate and require an additional hypothesis as, with the measured directions, one shear stress cannot be determined—the one on the surface of the specimen. To solve this, the hypothesis would need to neglect it, assume that it would be equal to another with the actual data, or involve making additional measurements at ϕ 45 and 135°; all of these would require time for measurements and data analysis. This point must be considered when designing the experiment, as the shear stress level can only be determined during data analysis (i.e., after the experiment). It can be carried out at some points along the depth, but currently not all of them.

5. Conclusions

In conclusion, this study examined residual stresses in industrial multilayer structures produced by atmospheric plasma spraying (APS). Through the use of the high-energy X-ray diffraction method (HEXRD), precise measurements were taken across the entire thickness of these structures. The results revealed stable stress levels in individual phases when the considered position was far from the interfaces, but significant variations were observed near these interfaces between materials. The results close to the interface are difficult to interpret due to geometric (different convoluting, diffracting spots) and chemical effects (element diffusion affects the lattice parameters). It is crucial to note that the isotropic assumptions underlying the $\sin^2\psi$ method are not always valid for multilayer materials, especially near interfaces. Therefore, a thorough understanding of the microstructures and properties of materials at different scales is necessary in order to accurately interpret X-ray diffraction data and evaluate residual stresses.

This study highlights that the HEXRD and $\sin^2\psi$ methods allow us to determine the stress tensor in fine-layered materials. In a previous study [24], a similar methodology was applied to bulk material. The detailed methodology therein can be generalized to several materials upon which the HEXRD method can be applied. With progress in the field of synchrotron sources, it will be possible to use very fine beams to more accurately follow stress evolution at the interfaces.

Moreover, the methodology used for HEXRD data analysis involves handling a considerable volume of raw data and requires that careful attention be paid to data selection and verification. Despite the challenges associated with the quantity of data, the $\sin^2\psi$ method provides a robust approach for determining stresses in individual phases of multilayer structures.

Furthermore, this study highlighted the importance of accurately determining stress-free parameters to assess absolute stresses in materials. Variations in material microstructures, such as the phases and any evolutions induced by industrial processes, can affect the stress-free parameters, emphasizing the need for a careful evaluation of these parameters.

Finally, our analysis of mechanical anisotropy and diffraction peak selection underscored the significance of these factors in accurately interpreting X-ray diffraction data. The choices of mechanical anisotropy models and diffraction peaks can have a significant impact on the determined stress levels.

In summary, this study provides valuable insights into the methodology and analytical considerations necessary for evaluating residual stresses in multilayer structures in order to better understand the charge transfer between layers produced by APS. A thorough understanding of material microstructures and careful consideration of parameter and model selection are essential for accurately interpreting X-ray diffraction data and evaluating residual stresses in these complex systems.

Author Contributions: Conceptualization, G.G. and B.M.; methodology, G.G.; software, G.G.; validation, B.M., P.A., S.S. and Q.P.d.; formal analysis, G.G.; investigation, G.G., S.S., Q.P.d. and B.M.; resources, P.A., S.S. and Q.P.d.; data curation, G.G.; writing—original draft preparation, G.G.; writing—review and editing, G.G. and B.M.; visualization, G.G.; validation, B.M., P.A., S.S. and Q.P.d.; supervision, S.S.; project administration, S.S.; funding acquisition, B.M. All authors have read and agreed to the published version of the manuscript.

Funding: This research was funded by SAFRAN aircraft engines (ex SNECMA).

Data Availability Statement: Data are not a available at the moment.

Acknowledgments: The HEXRD experiments were conducted at the ESRF ID11 and ID22 beamlines in Grenoble under the IN876 project. ESRF is acknowledged for providing the beamtime and beamline staff are acknowledged for their help during the experiments.

Conflicts of Interest: Authors Patrick Adenis and Quentin Pujol d'Andredo were employed by the company SAFRAN Aircraft Engines, author Serge Selezneff was employed by the company SAFRAN Tech. The remaining authors declare that the research was conducted in the absence of any commercial or financial relationships that could be construed as a potential conflict of interest.

Abbreviations

The following abbreviations are used in this manuscript:

APS	Atmospheric Plasma Spraying
CTE	Thermal Expansion Coefficient
ESRF	European Synchrotron Radiation Facility
FWHM	Full Width at Half Maximum
HEXRD	High-Energy X-ray Diffraction
Ti64	Ti-6Al-4V Alloy
XEC	X-ray Elastic Coefficients
XRD	X-ray Diffraction

References

1. Clyne, T.; Gill, S. Residual stresses in thermal spray coatings and their effect on interfacial adhesion: A review of recent work. *J. Therm. Spray Technol.* **1996**, *5*, 401–418. [CrossRef]
2. Sampath, S.; Jiang, X.; Matejicek, J.; Prchlik, L.; Kulkarni, A.; Vaidya, A. Role of thermal spray processing method on the microstructure, residual stress and properties of coatings: An integrated study for Ni–5 wt.%Al bond coats. *Mater. Sci. Eng. A* **2004**, *364*, 216–231. [CrossRef]
3. Kuroda, S.; Clyne, T. The quenching stress in thermally sprayed coatings. *Thin Solid Films* **1991**, *200*, 49–66. [CrossRef]
4. Mortensen, A.; Suresh, S. Functionally graded metals and metal-ceramic composites: Part 1 Processing. *Int. Mater. Rev.* **1995**, *40*, 239–265. [CrossRef]
5. Suresh, S.; Mortensen, A. Functionally graded metals and metal-ceramic composites: Part 2 Thermomechanical behaviour. *Int. Mater. Rev.* **1997**, *42*, 85–116. [CrossRef]
6. Cherradi, N.; Delfosse, D.; Ilschner, B.; Kawasaki, A. Functional gradient materials: Application of the concept, production techniques by powder metallurgy. *Rev. Met. Paris* **1996**, *93*, 185–196. [CrossRef]
7. Delfose, D.; Kunzi, H.; Ilschner, B. Expermental determination of residual stresses in materials with a one dimensional gradient of composition. *Acta Metall. Mater.* **1992**, *40*, 2219–2224. [CrossRef]

8. Rossini, N.; Dassisti, M.; Benyounis, K.; Olabi, A. Methods of measuring residual stresses in components. *Mater. Des.* **2012**, *35*, 572–588. [CrossRef]
9. Denkena, B.; Dreier, S. Simulation of Residual Stress Related Part Distortion. In *Proceedings of the New Production Technologies in Aerospace Industry*; Denkena, B., Ed.; Springer int Publishing AG, Lecture Notes in Production Engineering; Springer: Cham, Swizerland, 2013; pp. 105–113. [CrossRef]
10. Prime, M.B. Residual Stress Measurement by Successive Extension of a Slot: The Crack Compliance Method. *Appl. Mech. Rev.* **1999**, *52*, 75–96. [CrossRef]
11. Schajer, G.S.; Whitehead, P.S. *Hole-Drilling Method for Measuring Residual Stresses*; Springer: Charm, Swizerland, 2018. [CrossRef]
12. Wolf, I.D. Micro-Raman spectroscopy to study local mechanical stress in silicon integrated circuits. *Semicond. Sci. Technol.* **1996**, *11*, 139. [CrossRef]
13. Michaels, C.A.; Cook, R.F. Determination of residual stress distributions in polycrystalline alumina using fluorescence microscopy. *Mater. Des.* **2016**, *107*, 478–490. [CrossRef] [PubMed]
14. Fitzpatrick, M.E.; Fry, A.T.; Holdway, P.; Kandil, F.A.; Shackleton, J.; Suominen, L. Determination of Residual Stresses by X-ray Diffraction. Measurement Good Practice Guide. 52. 2005. Available online: https://eprintspublications.npl.co.uk/2391/ (accessed on 20 May 2024).
15. Besnard, A.; Ardigo, M.; Imhoff, L.; Jacquet, P. Curvature radius measurement by optical profiler and determination of the residual stress in thin films. *Appl. Surf. Sci.* **2019**, *487*, 356–361. [CrossRef]
16. Prabith, K.; Krishna, I.R.P. Response and stability analysis of a two-spool aero-engine rotor system undergoing multi-disk rub-impact. *Int. J. Mech. Sci.* **2022**, *213*, 106861. [CrossRef]
17. Darut, G. Elaboration de Revêtements à Structure Sub-Micrométrique Pour Applications Tribologiques par Projection Plasma de Suspensions. Ph.D. Thesis, Université de Limoges, Limoges, France, 2010.
18. Fauchais, P. Understanding plasma spraying. *J. Phys. D Appl. Phys.* **2004**, *37*, R86. [CrossRef]
19. Burtin, P. Transformation des Alumines de Transition en Alumine Alpha, Influence d'élÉments Étrangers sur la Stabilité des Alumines. Ph.D. Thesis, Ecole des Mines de Saint-Etienne, Saint-Etienne, France, 1985.
20. Oukach, S.; Hamdi, H.; El Ganaoui, M.; Pateyron, B. Numerical study of the spreading and solidification of a molten particle impacting onto a rigid substrate under plasma spraying conditions. *Therm. Sci.* **2015**, *19*, 277–284. [CrossRef]
21. Fauchais, P.; Vardelle, A. Thermal Spray Coatings. In *Wiley Encyclopedia of Electrical and Electronics Engineering*; John Wiley & Sons, Ltd: Hoboken, NJ, USA, 2007. [CrossRef]
22. pyFAI Documentation. Available online: https://www.silx.org/doc/pyFAI/latest/pyFAI.htm (accessed on 20 May 2024)
23. Kieffer, J.; Valls, V.; Blanc, N.; Hennig, C. New tools for calibrating diffraction setups. *J. Synchrotron Radiat.* **2020**, *27*, 558–566. [CrossRef]
24. Geandier, G.; Vautrot, L.; Denand, B.; Denis, S. In Situ Stress Tensor Determination during Phase Transformation of a Metal Matrix Composite by High-Energy X-ray Diffraction. *Materials* **2018**, *11*, 1415. [CrossRef] [PubMed]
25. Hauk, V. *Structural and Residual Stress Analysis by Nondestructive Methods*; Elsevier Science: Amsterdam, The Netherlands, 1997. [CrossRef]
26. Mejri, M. Caractérisation des Propriétés Thermomécaniques de Matériaux Utilisés pour la Fabrication de Modules Thermo-Électriques et Modélisation par Éléments Finis de leur Comportement en Usage. Ph.D. Thesis, Université de Toulouse 3, Toulouse, France, 2020.
27. Slim, M.F.; Geandier, G.; Malard, B.; Rouillard, F. Microstructural and Chemical Changes of a Ti-Stabilized Austenitic Stainless Steel After Exposure to Liquid Sodium at Temperatures Between 500 °C and 650 °C. *Metall. Mater. Trans. A* **2021**, *52*, 4438 – 4453. [CrossRef]
28. Slim, M.F.; Geandier, G.; Rouillard, F.; Malard, B. Determination of residual stress gradient in a Ti-stabilized austenitic stainless steel cladding candidate after carburization in liquid sodium at 500 °C and 600 °C. *Acta Mater.* **2021**, *221*, 117435. [CrossRef]
29. Heidelbach, F.; Riekel, C.; Wenk, H.R. Quantitative texture analysis of small domains with synchrotron radiation X-rays. *J. Appl. Crystallogr.* **1999**, *32*, 841–849. [CrossRef]
30. ID 22 Web Site ESRF (Grenoble, France). Available online: https://www.esrf.fr/id22 (accessed on 20 May 2024)
31. Gallas, M.R.; Piermarini, G.J. Bulk Modulus and Young's Modulus of Nanocrystalline γ-Alumina. *J. Am. Ceram. Soc.* **1994**, *77*, 2917–2920. [CrossRef]
32. Rezai, C. Internal Report—Université de Toulouse—Measurement by Acoustic Resonnace. 2014.
33. SNECMA. Internal Discussions. 2015.
34. Fan, Z. On the young's moduli of Ti-6Al-4V alloys. *Scr. Metall. Mater.* **1993**, *29*, 1427–1432. [CrossRef]
35. ID 11 Web Site ESRF (Grenoble, France). Available online: https://www.esrf.fr/id11 (accessed on 20 May 2024)
36. Murray, C.E. Equivalence of Kröner and weighted Voigt-Reuss models for x-ray stress determination. *J. Appl. Phys.* **2013**, *113*, 153509. [CrossRef]

Disclaimer/Publisher's Note: The statements, opinions and data contained in all publications are solely those of the individual author(s) and contributor(s) and not of MDPI and/or the editor(s). MDPI and/or the editor(s) disclaim responsibility for any injury to people or property resulting from any ideas, methods, instructions or products referred to in the content.